A Novel Ultrafast Transient Constant ON-Time Buck Converter for Multiphase Operation

Wen-Chin Liu, *Student Member, IEEE*, Ching-Hsiang Cheng, Chunting Chris Mi, *Fellow, IEEE*, and Patrick P. Mercier, *Senior Member, IEEE*

***Abstract*—Constant ON-time control (COT) has been widely adopted in buck converters because of its simplicity, fast transient response, and high light-load efficiency. However, the increasing power demands of CPUs and AI/ML engines is pushing voltage regulators to support higher output currents, which typically requires the use of multiphase operation. However, since most high-performance COT schemes utilize ripple as a control variable, the ripple cancellation point in multiphase designs imposes difficult stability concerns, limiting performance, and robustness. In this article, a novel ultrafast transient COT (UFTCOT) control scheme is proposed to enable fast and robust operation even in multiphase converters. The small-signal models of the proposed control scheme are derived based on a describing function technique, whose theoretical results are compared, along with simulation and measurement results, to contrast the proposed UFTCOT technique to exiting approaches.**

***Index Terms*—Constant ON-time (COT), describing function (DF), fast transient, multiphase operation, small-signal modeling.**

I. Introduction

THE dynamic power demands of central processing units (CPUs) and neural network processors continue to increase, putting increasing pressure on dc–dc-converting voltage regulators (VRs) to supply a clean, low-ripple voltage at high efficiency across a wide dynamic range of wildly varying current loads. A representative CPU load profile is shown in Fig. 1, illustrating that while the CPU is often in a light load condition consuming only a few watts (or less), it does occasionally, in the span of a few microseconds (or less), transition to a turbo mode where it consumes a few hundred watts. As a result of this typical operation, VRs need to have high efficiency at light load for idle operation, fast transient response for the short transition between idle and turbo modes, and high current capability at high efficiency for turbo mode power requirements. Simultaneously being nimble to varying loads over a large dynamic range, while keeping efficiency high and voltage regulation stable is a known difficult challenge in the power electronics community.

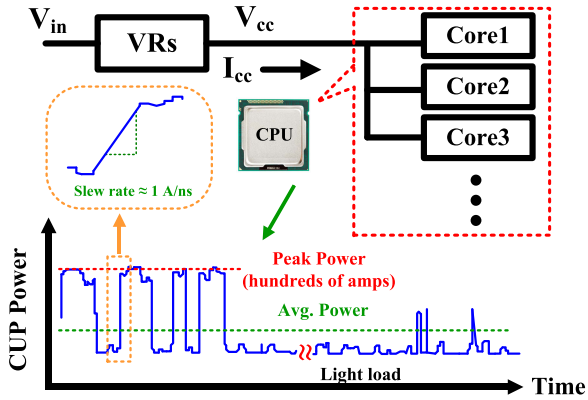

Fig. 1. Representative transient power demands of modern CPUs.

One of the more popular control technique to attempt to deal with this problem is the constant ON-time (COT) technique. Here, the top power NMOS transistor in a buck converter is always turned ON for a constant amount of time every cycle regardless of load conditions, which is in contrast to conventional constant frequency approaches. Under light-load operations, COT control inherently reduces its switching frequency, hence increasing overall conversion efficiency at such loads. For example, the conversion efficiency of COT-controlled buck converter can be as high as 80% at light-load compared to around 30% with equivalent constant frequency control [1], [2]. Consequently, COT control has been widely adopted in consumer electronic devices.

COT-based control techniques also offer advantageous operation in response to high slew rate load steps (e.g., up to 1000 A/μs) due to its high-bandwidth design achievability, and in some cases, ultralow susceptibility to load transient. While there are multiple COT variants [3], [4], ripple-based COT (RBCOT) control schemes have captured the most attention due to their simplicity and inherent high-load-transient immunity. However, RBCOT control schemes suffer from subharmonic oscillations if multilayer ceramic capacitors are used as output

Manuscript received November 3, 2020; revised February 5, 2021; accepted April 22, 2021. Date of publication April 28, 2021; date of current version July 30, 2021. Recommended for Publication by Associate Editor L. Corradini. *(Corresponding author: Wen-Chin Liu.)*

Wen-Chin Liu is with the Department of Electrical and Computer Engineering, University of California, San Diego, CA 92093 USA, and also with the Department of Electrical and Computer Engineering, San Diego State University, San Diego, CA 92182 USA (e-mail: brianliu.pe@gmail.com).

Ching-Hsiang Cheng is with the Department of Electrical Engineering, National Taiwan University, Taipei 10617, Taiwan (e-mail: wind19871219@gmail.com).

Chunting Chris Mi is with the Department of Electrical and Computer Engineering, San Diego State University, San Diego, CA 92182 USA (e-mail: mi@ieee.org).

Patrick P. Mercier is with the Department of Electrical and Computer Engineering, University of California, San Diego, CA 92093 USA (e-mail: pmercier@ucsd.edu).

Color versions of one or more figures in this article are available at https://doi.org/10.1109/TPEL.2021.3076430.

Digital Object Identifier 10.1109/TPEL.2021.3076430

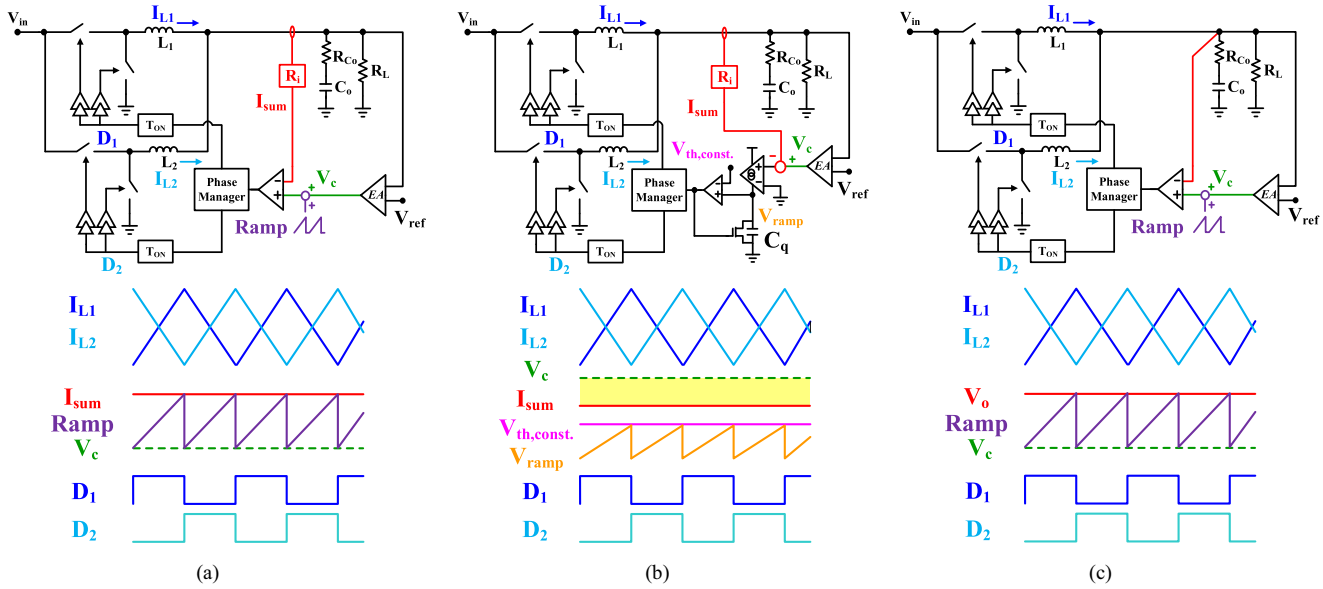

Fig. 2. Circuit diagrams and modulation waveforms. (a) CMCOT. (b) IQCOT. (c) RBCOT.

capacitors, and hence, external ramp generators [5]–[7] are typically required to stabilize the system, sacrificing droop and response time to load steps.

In addition to light-load efficiency and large load step control concerns, simply operating buck converters at high output power is challenging. To help, multiphase operation, where power is delivered through a network of time-interleaved inductors, can increase the total output power capabilities while simultaneously leveraging the multiphase operation for reduced ripple. However, ripple reduction can be a double-edged sword if COT control is desired, since most COT control schemes rely on the current/voltage ripple to achieve modulation. As a result, multiphase COT schemes again typically require an external ramp waveform for stable control, increasing design complexity and sacrificing performance.

To address these issues, this article proposes a COT control scheme that combines three feedback loops, namely a capacitor–current loop, an output voltage threshold loop, and an output voltage regulation loop, together with a self-generated ramp function proportional to both capacitor current and output voltage, to achieve a fast-transient response in a manner that is compatible with low-complexity multiphase operation. The article is organized as follows: a review of conventional multiphase and COT control schemes is provided in Section II, while the proposed circuit architecture is presented and discussed in Section III. Small-signal models are demonstrated in Section IV, while simulations and experimental results are provided in Section V. Finally, Section VI concludes the article.

II. Review and Analysis of Existing Control Schemes

In this section, three different multiphase control schemes will be discussed: current-mode COT (CMCOT), inverse-charge COT (IQCOT), and ripple-based COT (RBCOT). The small-signal models for each approach will be derived, facilitating direct comparison of the control-to-output transfer functions and of the output impedances.

A. Control Laws for CMCOT, IQCOT, and RBCOT

1) Current Mode COT: The CMCOT control scheme, shown in Fig. 2(a), possesses two feedback loops: 1) the inner loop is the current sensing loop, converting the summed current I_{sum} from the two inductor phases into a voltage signal via R_i fed to the negative terminal of the comparator; and 2) the outer loop is a voltage feedback loop converting the error signal between the output voltage and a reference voltage into a control voltage V_c fed to the positive terminal of the comparator. Once the sensed $I_{sum} \times R_i$ reaches V_c, the phase manager is triggered and determines the turn-ON instance of each phase. That is, this control utilizes the sum current ripple in modulation. However, as shown in Fig. 2(a), the sum current ripple is eliminated at the ripple cancellation point (i.e., when both inductors are perfectly out of phases), and hence the modulation cannot be achieved merely by the current ripple, leading to system instability at this important operating point. To prevent an unstable condition and to improve noise immunity at the ripple cancellation point, an external ramp which is purposefully added to V_c to avoid this issue is required under multiphase operation.

2) Inverse-Charge COT: Compared to CMCOT control, IQCOT control is inherently suitable for multiphase operation because the ramp generation process is built directly into the feedback loop design. As shown in Fig. 2(b), the control voltage V_c is generated from error amplifier, which is then subtracted by sensed inductor current. The voltage difference between the control signal and the sensed current is fed into a transconductor that generates a proportional current used to charge capacitor C_q. Then, the voltage across C_q is fed to the positive terminal of the comparator and compared with a constant threshold voltage $V_{th,const.}$ to determine the turn-ON instance for each phase. Owing to the charging process in the modulation loop, the system

can properly operate in a multiphase circuit, even when the two inductors are operating perfectly out of phase for maximum ripple reduction, as shown in Fig 2(b). Besides, the inverse charge method supports better noise immunity than conventional charge control [8].

3) Ripple-Based COT: The RBCOT control scheme is illustrated in Fig. 2(c). Its modulation law is very similar to CMCOT, in the sense that the output voltage is compared to a reference voltage, generating an error control signal V_c, to which an external ramp signal is added prior to reaching the positive terminal of the comparator. Unlike CMCOT, however, instead of sensing the summed current, the output voltage is directly driven to the negative terminal of the comparator. A major benefit of voltage sensing is that the modulator can respond to load transient immediately, and as a result, RBCOT can have the best load transient response performance. However, since the output voltage consists of the capacitor voltage ripple and the equivalent series resistor (ESR) voltage ripple, the phase delay issue between the capacitor voltage and the output voltage might result in subharmonic oscillations. Moreover, similar to CMCOT control, the interleaving operation further degrades stability due to ripple cancellation, as shown in Fig. 2(c), which is why an external ramp is again required to address stability concerns.

B. Control-to-Output Transfer Function

The control-to-output transfer function $G_{vc}(s)$ of CMCOT control with an external ramp is shown in (1), while the plots can be found in [9] and [10]. From (1), it can be seen that an additional pair of conjugate zeros and poles are introduced due to external ramp compensation. Since $Q_1 = 2/\pi$, $\omega_1 = \pi/T_{on}$, and $\omega_2 = \pi/T_{sw}$, the frequency and Q-value of the conjugate zeros are constant and independent of the external ramp's slope. In contrast, the Q-value of the additional conjugate poles vary with the slope of the external ramp. In practice, the slope of the external ramp should not be large in order to prevent extra low-frequency phase drop caused by the split poles. As a result, the complex poles and zeros can approximately cancel each other, and thus the loop gain can be efficiently designed to achieve a high bandwidth because only a single pole dominates. Besides, unlike other COT-based controls (i.e., RBCOT and IQCOT) whose conjugate poles at $\omega_2 = \pi/T_{sw}$ in $G_{vc}(s)$ might move to right-half plane (RHP) because of a negative Q-value, causing system instability, there are no stability concerns even when an external ramp is applied in CMCOT because the Q-value of the conjugate poles at $\omega_2 = \pi/T_{sw}$ is always a positive value.

The $G_{vc}(s)$ of the IQCOT control [11], described in (2), is similar to CMCOT but without the conjugate zeros. Besides, the quality factor Q_3 at ω_2 in IQCOT control is different from the quality factor Q_2 in CMCOT control, where ω_2 is equal to half-switching frequency $f_{\rm sw}/2$. Obviously, the complex pole at $f_{sw}/2$ may cause the stability issue if Q_3 becomes a negative value, and thus the stability of this control technique depends strongly on the control stage parameters. In addition, owing to the complex poles, there is an extreme phase drop that appears at $f_{sw}/2$. As a consequence, compared to CMCOT, the design of the loop gain bandwidth will be limited. Yet, this control does not require an external ramp; hence, $G_{vc}(s)$ for multiphase will have the same $G_{vc}(s)$ as a single-phase design, which is a nice benefit. Note that the plot for $G_{vc}(s)$ for IQCOT control is shown in [11].

Equation (3) shows $G_{vc}(s)$ of RBCOT control, and its graphical illustration is shown in [5]. As can be readily seen, $G_{vc}(s)$ here is by far the most complicated one, and since it is not easy to separate the poles and zeros, it is difficult to analyze and design well. According to [10], if a large external ramp is applied to this control technique, it will cause gain peaking at both low and high frequencies, which seriously degrade the achievable bandwidth. Conversely, a small external ramp causes an unstable condition. Hence, a proper external ramp design is essential in this control scheme to achieve high bandwidth and stable performance. Generally, the external ramp design is recommended as 2–6 times falling slope of the sensed inductor current [10]

$$\frac{\hat{v}_o(s)}{\hat{v}_{c,CM}(s)} \approx K_c \frac{(R_{Co}C_o s+1)}{s/\omega_a+1} \frac{1}{1+\frac{s}{Q_1\omega_1}+\frac{s^2}{\omega_1^2}} \times \left(\frac{1+\frac{s}{Q_1\omega_2}+\frac{s^2}{\omega_2^2}}{1+\frac{s}{Q_2\omega_2}+\frac{s^2}{\omega_2^2}}\right) \tag{1}$$

$$\frac{\hat{v}_o(s)}{\hat{v}_{c,IQ}(s)} \approx K_c \frac{(R_{Co}C_o s+1)}{s/\omega_a+1} \frac{1}{1+\frac{s}{Q_1\omega_1}+\frac{s^2}{\omega_1^2}} \frac{1}{1+\frac{s}{Q_3\omega_2}+\frac{s^2}{\omega_2^2}} \tag{2}$$

$$\frac{\hat{v}_o(s)}{\hat{v}_{c,RB}(s)} \approx \frac{R_{Co}C_o s+1}{1+\frac{s}{Q_1\omega_1}+\frac{s^2}{\omega_1^2}} \times \frac{\left(1+\frac{s}{Q_1\omega_2}+\frac{s^2}{\omega_2^2}\right)}{\left(1+\frac{s}{Q_4\omega_2}+\frac{s^2}{\omega_2^2}\right)\left(1+\frac{s}{Q_1\omega_2}+\frac{s^2}{\omega_2^2}\right)+\frac{S_e}{S_f}R_{Co}C_oT_{sw}s^2} \tag{3}$$

where

$$K_c = \frac{R_L}{R_i\left(1-R_L\times k_2\right)}$$

$$\omega_a = \frac{1-R_L\times k_2}{\left(R_L+R_{C_o}\right)C_o - R_L R_{C_o}C_o\times k_2}$$

$$k_{2(CMCOT)} = -\frac{1}{2}\frac{T_{on}R_i}{L_s} \quad k_{2(IQCOT)} = -\frac{C_T}{g_m}\frac{V_{th,const.}}{V_{in}R_iT_{on}}$$

$$\omega_1 = \pi/T_{on} \qquad \omega_2 = \pi/T_{sw} \qquad Q_1 = 2/\pi$$

$$Q_2 = \frac{1}{\pi\left(\frac{1}{2}+\frac{S_e}{S_f}\right)} \qquad Q_3 = \frac{2s_fT_{on}}{\pi D\left(\frac{2C_TV_{th,const}D}{g_mT_{on}}-s_fT_{on}\right)}$$

$$Q_4 = \frac{T_{sw}}{\pi\left(R_{Co}C-\frac{T_{on}}{2}\right)} \qquad s_f = R_i\frac{V_o}{L_s}.$$

C. Output Impedance of CMCOT, IQCOT, and RBCOT

The output impedance $Z_o(s)$ between CMCOT and IQCOT control approaches are fairly similar because both of them are current-mode-based control and affected by k_2 term, where k_2

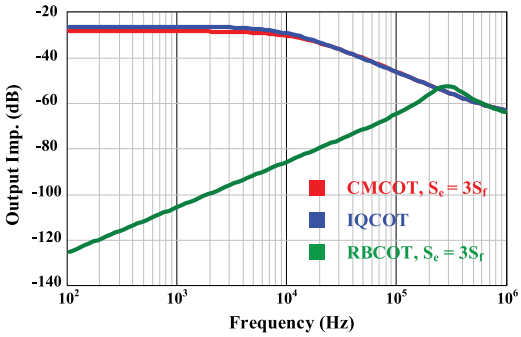

Fig. 3. Output impedance comparison for CMCOT, IQCOT, and RBCOT.

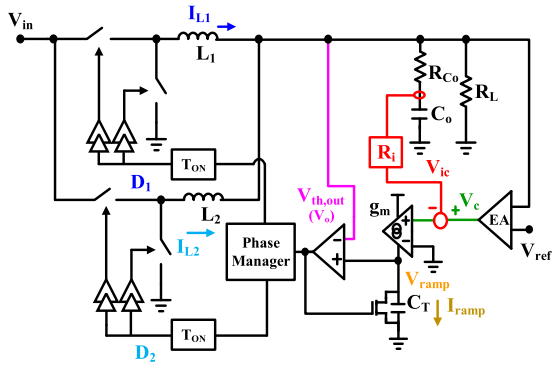

Fig. 4. Circuit diagram of the proposed control scheme for a buck converter.

term is defined as a transfer function from the output voltage to the inductor current. Because the inductor current can be viewed as an ideal current source under current-mode-based control, the output impedance will be equal to the impedance converting the inductor current into an output voltage. Hence, the output impedance can be obtained from the output network and k_2. Finally, the output impedance is the output network in parallel with the negative reciprocal of k_2 [12], as shown in (4). In RBCOT control, the feedback loop is slightly different compared to the others because the feedback signal is not a current but a voltage. The output impedance $Z_o(s)$ is shown in (5), where $G_{vc}(s)$ is illustrated in (3).

Fig. 3 shows the frequency response of $Z_o(s)$ with different control schemes, where the external ramp magnitude in CMCOT and RBCOT control is set to three times the falling slope of the sensed inductor current. From Fig. 3, it can be seen that CMCOT and IQCOT are almost overlapped with each other, and RBCOT is far lower than the others. Thus, RBCOT control has by far the best load transient performance among them

$$Z_o(s) = \left(\frac{-1}{k_2} // \frac{R_L \left(R_{Co} C_o s + 1 \right)}{\left(R_L + R_{Co} \right) C_o s + 1} \right) \tag{4}$$

$$Z_o(s) \approx \left(G_{vc}(s) - 1 \right) \frac{R_{Co} C_o s + 1}{C_o s}. \tag{5}$$

D. Comments

In multiphase operation, both CMCOT and IQCOT control are easier to design than RBCOT control. However, these conventional current-mode-based control schemes suffer from fairly slow transient response due to inductor current sensing. On the other hand, RBCOT has the best transient response capability due to ultralow output impedance. Yet, the system design for RBCOT is a daunting task because of the ramp compensation required. Considering all the pros and cons in this section, a novel COT control is proposed to simultaneously enable inherent multiphase operation and fast transient response.

III. Proposed Ultrafast Transient COT Control Scheme

Fig. 4 shows the circuit diagram of the proposed control scheme for a two-phase buck converter. There are three feedback loops at work to perform modulation:

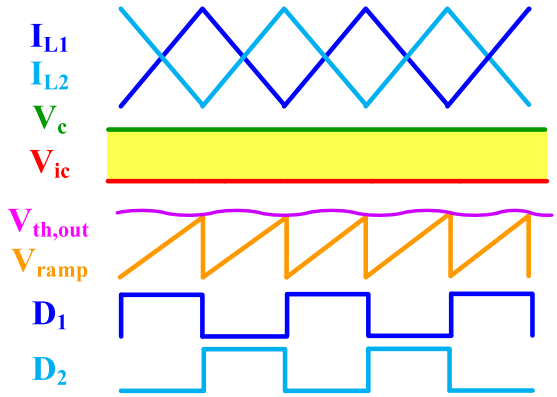

Fig. 5. Two-phase modulation waveforms under ripple cancellation point.

1) the first loop directly feeds the output voltage, which is also noted as output-voltage-threshold voltage $V_{th,out}$, back to the negative terminal of the comparator;
2) the second loop senses the capacitor current, converts it to a voltage and feeds it to a subtractor; and
3) the last loop feeds the output voltage into a high-gain compensator.

The reasons for each of these loop revisions will be discussed in the following paragraphs.

The detailed modulation waveforms under two-phase interleaving conditions are illustrated in Fig. 5. In modulation, the control signal V_c is generated from the error between the output voltage and the reference voltage V_{ref}. The control signal is then subtracted by the sensed capacitor current signal V_{ic}. Then, the difference will be converted into a ramp current I_{ramp} through a transconductor, which is used to charge capacitor C_T, generating a ramp voltage V_{ramp}. This ramp voltage is fed into the positive terminal of the comparator, and thus once it reaches the output-voltage-threshold voltage $V_{th,out}$ the phase manager is triggered, determining turn-ON instance, and a local feedback loop is temporarily activated to purge the charge on C_T, resetting V_{ramp} back to zero.

The quintessence of the modulation is the voltage difference between the control voltage and sensed capacitor current used to charge the threshold capacitor C_T forming a self-generated ramp. By providing feedback in this manner, the total charge built up on C_T in each cycle will be equal to the threshold

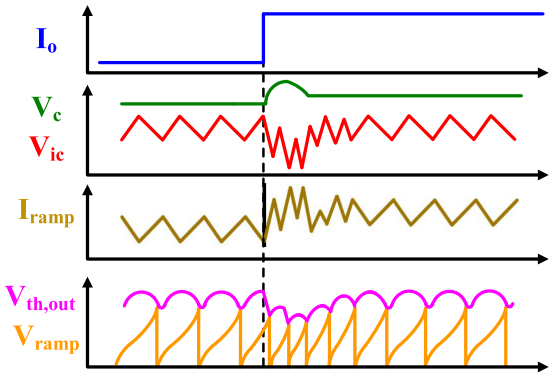

Fig. 6. Modulation waveform during load step-up transient.

voltage multiplied by C_T. According to the above idea, the current ripple in the capacitor current becomes insignificant since the control voltage V_c will adjust its value automatically to ensure that the total charge is constant over each cycle. One of the benefits of this charge control is that the converter can naturally operate at the ripple cancellation point in the multiphase application while maintaining normal operation without stability concerns or the need for an external ramp generator.

The difference between the inductor current and capacitor current feedback loop in COT-controlled Buck converters is extensively discussed in [13] and [14]. The literature uses frequency-domain analyses to show that the capacitor current sensing has a lower output impedance than the traditional inductor current sensing. In the time domain, the load current equals the inductor current minus the capacitor current. Therefore, when a load step-up transient occurs, the extra required load current will be provided by the capacitor since the inductor's current cannot change instantaneously. Instead, the capacitor current is capable of reflecting load transient instantaneously, which is why it is a favorable parameter to use for the purposes of load regulation. This is illustrated in Fig. 6, which shows the modulation waveform when a large load step-up transient occurs. Immediately after the load step-up, the sensed capacitor current V_{ic} drops, while the control voltage V_c increases simultaneously, causing the internally generated ramp current I_{ramp} to correspondingly increase. Then, according to the charge equation ($Q = C \times V = I \times T$), the time to reach the threshold voltage becomes shorter due to a larger voltage difference, significantly reducing response delay compared to inductor current sensing.

To further improve performance, the proposed control uses the output voltage as the threshold voltage instead of a constant voltage. The idea is very similar to RBCOT, which utilizes the feature that the output voltage changes instantly as load transients occur. As shown in Fig. 6, immediately after a load step-up the output voltage correspondingly drops, which in the proposed control law lowering the threshold voltage, further reducing charging time to reach the threshold voltage. All in all, the load transient response is improved remarkably with capacitor current sensing and direct output voltage feedback.

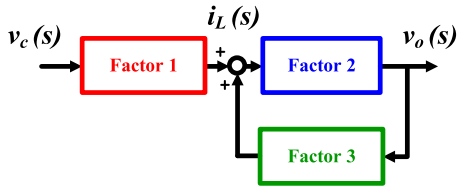

Fig. 7. Complete block diagram for current mode control scheme.

IV. Small-Signal Model and Frequency-Domain Analysis

The small-signal model (SSM) and stability criteria for the proposed control scheme will be derived and illustrated in this section. To simplify the derivation, a single phase condition is considered, and it can be easily extended to multiphase through the work in [15]. A describing function (DF) method [3], [4] will be applied for accurate modeling because, during SSM derivation, this approach considers the side-band components created by modulation. The developed SSM can be accurate all the way up to half the switching frequency.

A. Control-to-Output Transfer Function

To obtain a correct SSM, a complete current mode model can be first illustrated in Fig. 7 according to [3], which is composed of three blocks at work:

1) factor 1 represents the transfer function from the control voltage $v_c(s)$ to the inductor current $i_L(s)$;
2) factor 2 represents the transfer function from the inductor current $i_L(s)$ to the output voltage $v_o(s)$;
3) factor 3 represents the transfer function from the output voltage $v_o(s)$ back to the inductor current $i_L(s)$.

These blocks will be derived separately in the following paragraphs, and then the final SSM of the proposed control scheme can be derived through Mason's gain formula (MGF) and Fig. 7.

To obtain an accurate factor 1 and reduce complexity during derivation, the DF method is applied and simplified into few steps as follows:

1) assumptions;
2) OFF-time calculation from modulation waveforms;
3) Fourier analysis of duty cycle and inductor current; and
4) DF derivation.

Step 1 (Assumptions): There are three basic assumptions required before performing DF as follows: i) the slope of the inductor current is constant during ON-time and OFF-time intervals; ii) the amplitude of perturbation is much smaller than the perturbed signal (i.e., $V_c(t)$); iii) the switching frequency f_{sw} and the perturbation frequency f_m are commensurable.

Step 2 (OFF-Time Calculation from Modulation Waveforms): To illustrate how the perturbation affects the modulation, the modulation law of the proposed control scheme is first developed via Fig. 8. Here, the control voltage v_c is perturbed by a small sinusoidal perturbation with frequency f_m, which can be expressed as (6). It can be seen that the modulation points are varied with perturbation, namely, the turn-ON and turn-OFF instances change with the sinusoidal perturbation, where

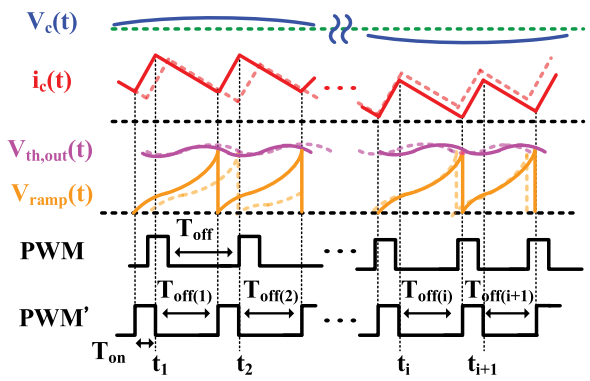

Fig. 8. Modulation law for the proposed control scheme.

PWM is the steady-state duty ratio; PWM′ is the duty ratio after being perturbed; $T_{off(i)}$ is the OFF-time in the i_{th} cycle and $T_{off(i)} = T_{off} + \Delta T_{off(i)}$, where T_{off} is the steady-state OFF-time and $\Delta T_{off(i)}$ is the OFF-time perturbation in the i_{th} cycle; T_i is the accumulated time from the first end of the ON-time to the end of the ON-time in i_{th} cycle, which can be calculated as: $T_i = (i-1)(T_{on} + T_{off}) + \sum_{k=1}^{i-1} \Delta T_{off(k)}$.

With the modulation waveforms in place, the equation of the inverse charge modulation is shown in (7). Then, the perturbed control voltage (6) can be substituted into (7) to derive the OFF-time perturbation, as shown in (8)

$$v_c(t) = r_o + \hat{r} sin\left(2\pi f_m t\right), \ \hat{r} << r_o \tag{6}$$

$$\int_{t_{i-1}+T_{off(i-1)}}^{t_i+T_{off(i)}} \left[v_c(t) - \ i_c(t)R_i\right] dt = \frac{C_T V_{th,out}}{g_m} \tag{7}$$

$$\begin{aligned} &\left(\tfrac{C_T V_{th,out}}{g_m T_{sw}} + \tfrac{1}{2} s_f T_{off}\right) \Delta t_{off(i)} \\ &\quad + \left(T_{sw} s_f - \left(\tfrac{C_T V_{th,out}}{g_m T_{sw}} + \tfrac{1}{2} s_f T_{off}\right)\right) \Delta t_{off(i-1)} \\ &= \tfrac{\hat{r}}{\pi f_m} sin\left(\pi f_m \left(T_{on} + T_{off}\right)\right) \\ &\quad \times \left[sin\left(2\pi f_m \left[(i-2)\left(T_{on} + T_{off}\right) - \tfrac{T_{on} - T_{off}}{2}\right] - \theta\right)\right. \\ &\quad \left. - sin\left(2\pi f_m \left[(i-1)\left(T_{on} + T_{off}\right) - \tfrac{T_{on} - T_{off}}{2}\right] - \theta\right)\right] \end{aligned} \tag{8}$$

$$\begin{aligned} d(t)|_{0 \le t \le t_M + T_{off(M)} + T_{on}} = \sum_{i=1}^{M} &\left[u\left(t - t_i - T_{off(i)}\right)\right. \\ &\left. - u\left(t - t_i - T_{off(i)} - T_{on}\right)\right] \end{aligned} \tag{9}$$

$$i_L(t)|_{0 \le t \le t_M + T_{off(M)} + T_{on}} = \int_0^t \left[\frac{V_{in}}{L_s} d(t) - \frac{V_o}{L_s}\right] dt + i_{L0} \tag{10}$$

$$\begin{aligned} c_{m(i_L)} = &\frac{1}{N\pi} \frac{V_{in}}{L_s} e^{-j2\pi f_m T_{off}} \left(e^{-j2\pi f_m T_{on}} - 1\right) \\ &\left[\sum_{i=1}^{M} \left(e^{-j2\pi f_m (i-1) T_{sw}} \sum_{k=1}^{i} \Delta T_{off(k)}\right)\right]. \end{aligned} \tag{11}$$

Step 3 (Fourier Analysis of Duty Cycle and Inductor Current): According to the modulation waveforms, the perturbed duty cycle and inductor current can be derived as (9) and (10), respectively. Thereafter, Fourier analysis can be performed to derive the Fourier coefficient C_m of the inductor current at the perturbation frequency f_m. By substituting (9) into (10), C_m of the inductor current can be found as (11).

Step 4 (DF Derivation): Eventually, the perturbed off-time (8) can be substituted into (11) to obtain factor 1, as

$$\frac{i_L(s)}{v_c(s)} = \frac{V_o}{sL_s} \frac{1}{sT_{on}} \frac{\left(1 - e^{-sT_{on}}\right)\left(1 - e^{-sT_{sw}}\right)}{x + \left(T_{sw} s_f - x\right) e^{-sT_{sw}}} \tag{12}$$

where

$$x = \frac{C_T V_{th,out}}{g_m T_{sw}} + \frac{1}{2} s_f T_{off}.$$

The factor 2 is the output impedance looking from the inductor side, given by (13), which is just the output capacitor with ESR in parallel with the output resistor

$$\text{Factor2}(s) = \frac{R_L \left(R_{Co} C_o s + 1\right)}{\left(R_L + R_{Co}\right) C_o s + 1}. \tag{13}$$

Factor 3, also known as k_2, represents the effect of the output voltage on inductor current, as the slope of inductor current will vary with the value of the output voltage. Hence, it can be modeled as a feedback loop. Based on the result in [3], factor 3 can be obtained through an average derivation because factor 3 usually affects the low-frequency behavior (i.e., the low-frequency pole) only. The average derivation is described as

$$\left.\frac{\partial \langle i_L \rangle}{\partial V_o}\right|_{V_{in}=constant} = -\frac{C_T}{g_m} \frac{2V_{th,out}}{V_{in} R_i T_{on}} + \frac{1}{R_L}. \tag{14}$$

Now, by applying Mason's gain formula (MGF) and padé approximation, the control-to-output transfer function can be derived as

$$\frac{\hat{v}_o(s)}{\hat{v}_c(s)} \approx \frac{K_c}{s/\omega_a + 1} \frac{\left(R_{Co} C_o s + 1\right)}{1 + \frac{s}{Q_1 \omega_1} + \frac{s^2}{\omega_1^2}} \frac{1}{1 + \frac{s}{Q_2 \omega_2} + \frac{s^2}{\omega_2^2}} \tag{15}$$

where

$$K_c = \frac{R_L}{R_i \left(1 - R_L \times k_2\right)}$$

$$\omega_a = \frac{1 - R_L \times k_2}{\left(R_L + R_{C_o}\right) C_o - R_L R_{C_o} C_o \times k_2}$$

$$k_2 = -\frac{C_T}{g_m} \frac{2V_{th,out}}{V_{in} R_i T_{on}} + \frac{1}{R_L}$$

$$\omega_1 = \pi / T_{on} \qquad Q_1 = 2/\pi \qquad \omega_2 = \pi / T_{sw}$$

$$Q_2 = \frac{2 s_f T_{on}}{\pi D \left(\frac{2 C_T V_{th,out} D}{g_m T_{on}} - s_f T_{on}\right)} \qquad s_f = R_i \frac{V_o}{L_s}.$$

Here, s_f represents the sensed falling slope of the inductor current; R_i is the sensing gain; R_L is the load resistance; C_o

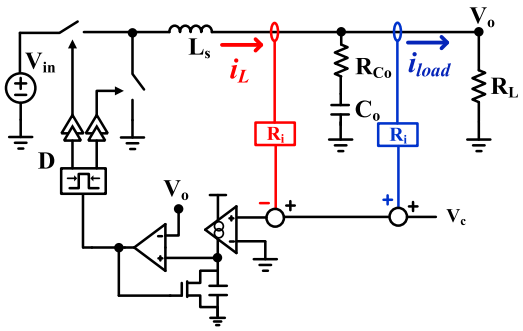

Fig. 9. Capacitor current loop decomposition.

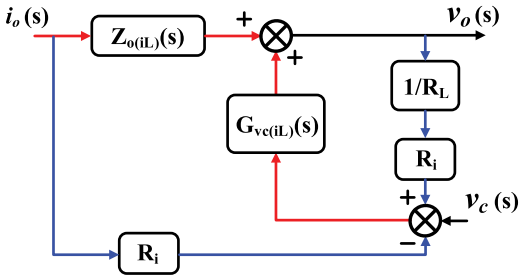

Fig. 10. Output impedance block diagram for the proposed control scheme.

and R_{Co} are the output capacitance and ESR, respectively; C_T is the threshold capacitor for the inverse charge process; g_m is the transconductance, converting voltage difference into ramp current I_{ramp}; and D denotes the duty cycle.

The control-to-output transfer function, as shown in (15), shows a low-frequency pole, two pairs of conjugate poles, an ESR-based zero, and a dc gain of K_c. It should be noted that the poles located at the half-switching frequency may move to the right-half plane (RHP) if Q_2 becomes negative. Thus, the stability criteria can be expressed as

$$\frac{C_T L_s}{R_i g_m T_{sw}} > \frac{T_{on}}{2}. \tag{16}$$

B. Output Impedance Transfer Function

To simplify the output impedance derivation [16], the capacitor current loop can be decomposed into a inductor current loop and a load current loop based on (17), and then the equivalent circuit can be redrawn as shown in Fig. 9. It can be noted that the circuit is analogous to the IQCOT control scheme if the load current loop is excluded. Thus, the output impedance of proposed control technique can be derived based on IQCOT control with the load current loop closed

$$I_c = I_L - I_{load}. \tag{17}$$

To include effects caused by the load current loop, a small-signal current perturbation can be injected into the output terminal of the Buck converter, and the equivalent block diagram is found as Fig. 10. In the figure, the red lines are the effects of the inductor current loop, and the blue lines are the effects of the load current loop. If the load current loop is omitted (i.e., considering the red lines only), the output impedance is $Z_{o(iL)}(s)$ since v_c is a constant value, which is zero in the small-signal analysis. Then, the load current loop can be taken into consideration, creating two additional paths, a forward path and a feedback path, to the block diagram. The forward path is from the sensing network, which directly feeds sensed load current to the modulator, while the feedback path is from the local feedback caused by the load resistance, which is also sensed by sensing gain R_i and fed back to the modulator.

With the block diagram in place, the output impedance of the proposed control technique can be derived in (18) via Fig. 10 and MGF, where $G_{vc(iL)}(s)$, and $Z_{o(iL)}$ are small-signal models only considering the inductor current loop. The expressions for $G_{vc(iL)}(s)$ and the $Z_{o(iL)}$ are shown in (2) and (4), while k_2 is shown in (19)

$$Z_o(s) \equiv \frac{v_{out}(s)}{i_o(s)} \approx \frac{R_i \cdot G_{vc(iL)}(\mathrm{s}) - Z_{o(iL)}(s)}{\frac{R_i}{R_L} \cdot G_{vc(iL)}(\mathrm{s}) - 1} \tag{18}$$

$$k_2 = -\frac{C_T}{g_m} \frac{2V_{th,out}}{V_{in} R_i T_{on}}. \tag{19}$$

C. Transfer Function Comparison

In this section, both the control-to-output transfer function and output impedance of IQCOT and the proposed control scheme will be discussed to verify the stability and load transient response performance. Since CMCOT and IQCOT control schemes are extensively discussed in Section II, which share similar forms in transfer function, CMCOT can be easily extended, and therefore, CMCOT is omitted in this section.

1) Control-to-Output Transfer Function: The main differences between IQCOT and the proposed control are the threshold voltage and current sensing, where the former adopts a constant threshold voltage and inductor current sensing method, while the latter control scheme employs an output-voltage-threshold voltage and capacitor current sensing approach. To investigate the effects of the feedback loop on the overall control of the circuit, the control-to-output transfer function $G_{vc}(s)$ should be discussed, which is a metric for designers to evaluate stability and design compensation circuits.

$G_{vc}(s)$ of IQCOT and proposed control technique is shown in (2) and (15) separately. The two expressions are very similar to each other, with the main differences being the value of k_2 and the quality factor at frequency ω_2. According to the SSM derivation of $G_{vc}(s)$ and k_2, it can be concluded that the quality factor difference mainly comes from the difference of threshold voltages, while k_2 difference results from both current sensing and threshold voltage differences. Also, the difference in k_2 leads to different dc gain k_c and the low-frequency pole ω_a. In contrast, the difference in the quality factor results in stability concerns. That is, when the quality factor becomes negative, the system becomes unstable.

In summary, the capacitor current sensing feedback affects the dc gain and the low-frequency pole; on the other hand, the output-voltage-threshold voltage affects the dc gain, the low-frequency pole, and stability.

The bode plot of the control-to-output transfer function is shown in Fig. 11. As shown, the dc gain and the low-frequency pole are different in both control schemes. As for the quality

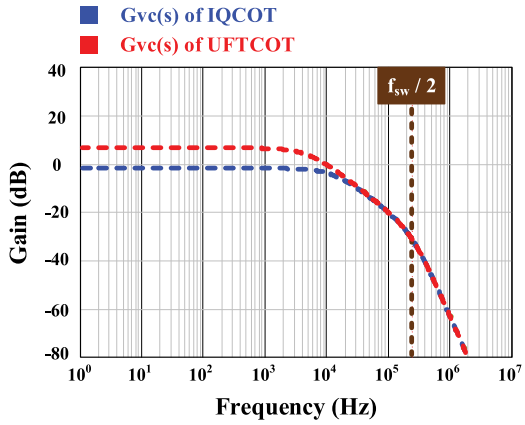

Fig. 11. Control-to-output transfer function comparison.

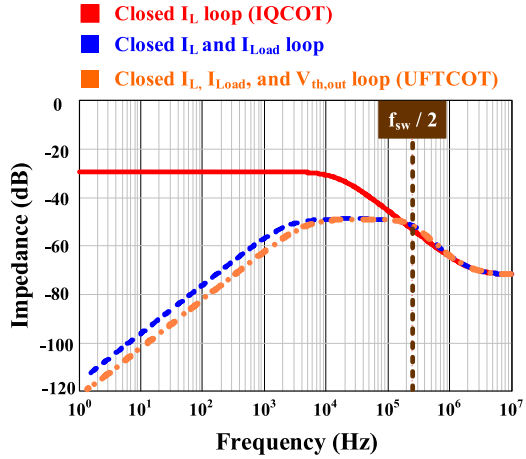

Fig. 12. Output impedance comparison.

factor at ω_2, if the dc value of the constant threshold voltage, which is IQCOT's threshold, and the output-voltage-threshold voltage, which is UFTCOT's threshold, are the same, the quality factor will be the same since the only difference in the quality factor expression is the threshold voltage. Therefore, the peaking at $f_{sw}/2$ is the same in Fig. 11.

2) Output Impedance: Apart from the loop effect on controls, the output impedance $Z_o(s)$ is also of interest for evaluating the load transient performance in the frequency-domain. Fig. 12 shows the impacts caused by the different feedback loops. As illustrated in Section IV-B, capacitor current sensing can be decomposed into inductor current feedback and load current feedback. Fig. 12 first shows $Z_o(s)$ with only the inductor current loop closed in red solid line, which is the same as IQCOT control. Then, when both the inductor current and load current loops are closed, as shown in blue dashed line, $Z_o(s)$ at low frequencies shows a ultralow impedance. This is a result from the capacitor current sensing, which behaves as a differentiator, reducing low-frequency impedance significantly. Finally, the orange dashed line shows $Z_o(s)$ with all loops closed, which is $Z_o(s)$ of proposed control technique. With additional output-voltage threshold loop, the impedance is further reduced. Hence, the proposed control can achieve a ultrafast load transient response.

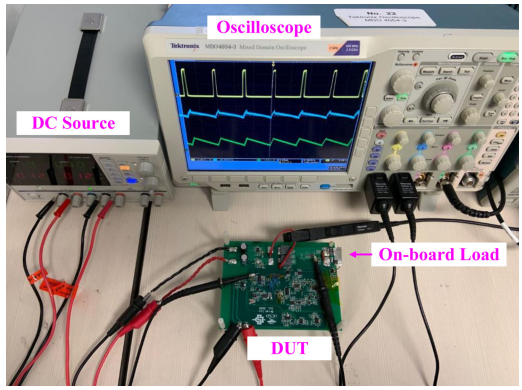

Fig. 13. Test bench setup for the proposed control scheme.

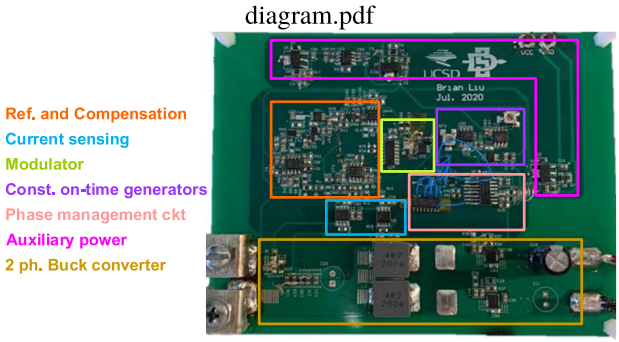

Fig. 14. Circuit implementation.

TABLE I
EXPERIMENTAL PARAMETERS

Parameters	Values
Input voltage range V_{in}	2.5-19 V
Output voltage range V_o	1.2 V
Output current range I_o	0 - 20 A
Switching frequency f_{sw}	$\approx$ 300 kHz
Output inductor L_s	4.7 μH
Output capacitor C_o	220 μF
Equivalent series resistance R_{Co}	10 mΩ
Threshold capacitor C_T	1 nF
Modulator transconductance g_m	8 mA/V
Sensing gain R_i	0.1 V/A

V. EXPERIMENTAL VERIFICATION

A. Circuit Implementation and Modulation Waveform

A two-phase buck converter is implemented in this work and designed in a way to support both a conventional IQCOT control technique, along with the proposed UFTCOT control technique. The test setup of the two-phase buck converter is shown in Fig. 13. A detailed implementation of the circuit is shown in Fig. 14, with a detailed schematic for the implementation shown in Fig. 15, and the experimental parameters are listed in Table I. In this article, a fully-discrete system is adopted for behavioral and SSM verification. An on-board load is adopted to achieve a fast load transient in order to ensure the performance of the loop is stressed under the most difficult of conditions without

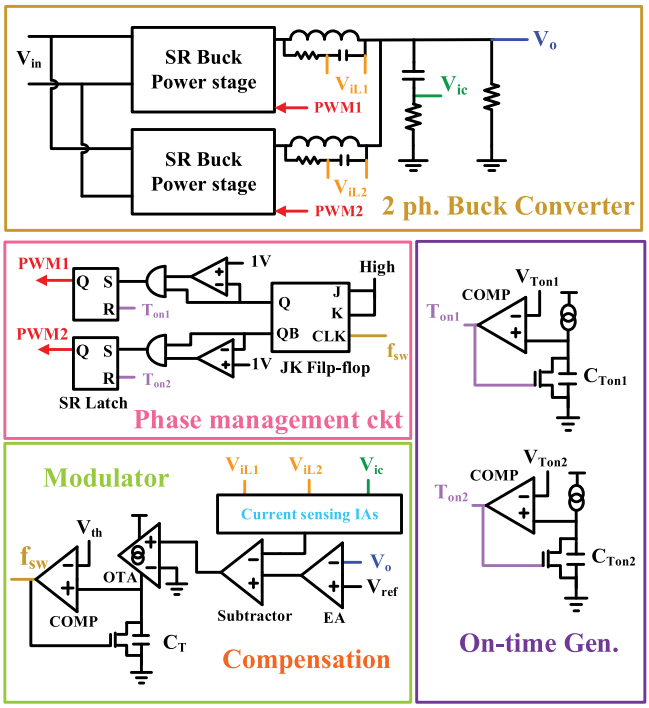

Fig. 15. Circuit schematic for the implementation.

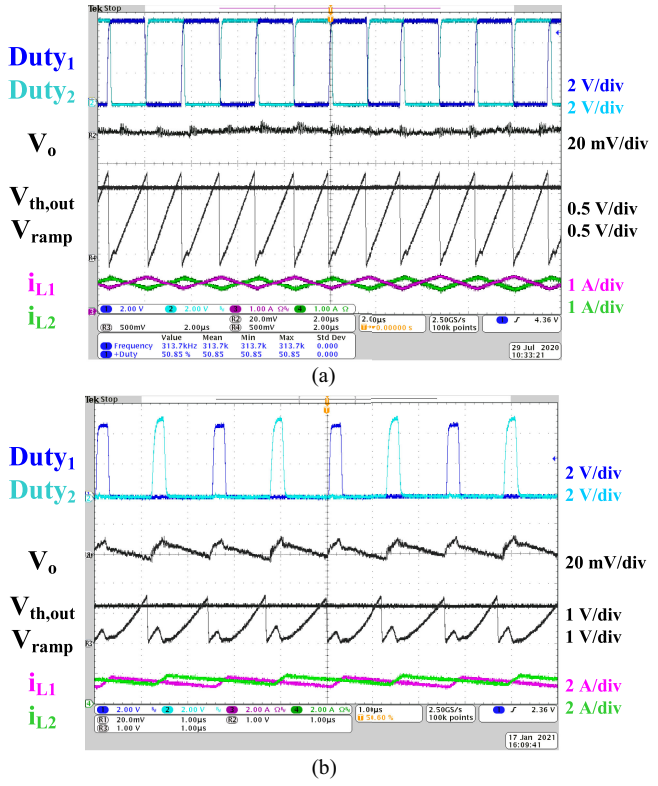

Fig. 16. Multiphase operation waveform of UFTCOT.

the effects of ringing due to the parasitics of connecting to an electronic load.

In the implemented circuit, owing to the limitation of discrete components, the switching frequency is set to 300 kHz, and a 4.7 μH inductor is chosen to ensure continuous-conduction mode (CCM) operation at this frequency. A simple capacitor current sensing technique is employed, which inserts a small series resistor in the capacitor path and senses the voltage across the resistor to simplify the implementation while verifying the behavior. This is why there is a relatively large ESR in Table I. There are several other more advances capacitor sensing techniques that could be employed in future work [17]–[19].

Design of the control stage parameters, i.e., g_m, R_i, and C_T, is limited by available discrete components. For example, g_m needs a compromise between maximum source current capability and its transconductance to prevent output saturation. For R_i, it requires a tradeoff between noise and circuit performance because the series resistor method is applied. That is, a small resistance may be sensitive to noise; on the other hand, a large resistance deteriorates load transient performance. Here, g_m and R_i are chosen as 8 mA/V and 0.1 V/A, respectively. Finally, C_T can be designed based on Q_2 in (15), where the recommended Q_2 is from 0.6 to 0.9 [20] to prevent an extra phase drop at low frequencies resulting from a low-Q value and an excessive peaking following by a high-Q value. In this work, Q_2 is designed to be 0.6 and C_T is therefore around 1 nF because the other variables, i.e., g_m and R_i, are already decided.

Altogether, both power stage and control stage design will vary depending on the implementation applied. For example, if an integrated-circuit implementation is employed, the switching frequency can be much higher, around 700 kHz to 1 MHz or even higher; therefore, the inductor size can be reduced significantly. Besides, an integrated current sensing technique can be used to prevent large ESR. For the control stage design, the value of g_m, R_i, and C_T will be limited by the process and topology of OTAs and sensors adopted. Still, the control design should be based on Q_2 in (15) to ensure a stable operation.

The two-phase modulation waveforms under different duty cycle conditions are shown in Figs. 16(a) and (b). As expected, the converter works well even when it operates at the ripple cancellation point where the duty cycle equals 50%, as shown in Fig. 16(a). Fig. 16(b) shows a low duty cycle situation and the ramp in modulation is a nonlinear ramp. It should be noted that because of the switching noise of sensed current, V_{ramp} experiences discharging when $Duty_{1,2}$ is turned OFF.

B. Small-Signal Model With Different Input Voltage

To validate the small-signal model proposed in Section IV, the control-to-output transfer function is measured under different input voltage conditions (12 and 5 V) while converting down to 1.2 V. The measurement is performed by a lock-in amplifier, which injects a small-signal perturbation with a dc bias to V_c terminal while disabling the error amplifier, and then measures the gain and phase from V_c to the output. Fig. 17(a) and (b) present the measurement results of the control-to-output transfer function, where the red lines are the calculation results as derived in the previous section, while the blue lines are the measurement results. As shown, the measurement results are well-matched with the calculation results for frequencies below $f_{sw}/2$.

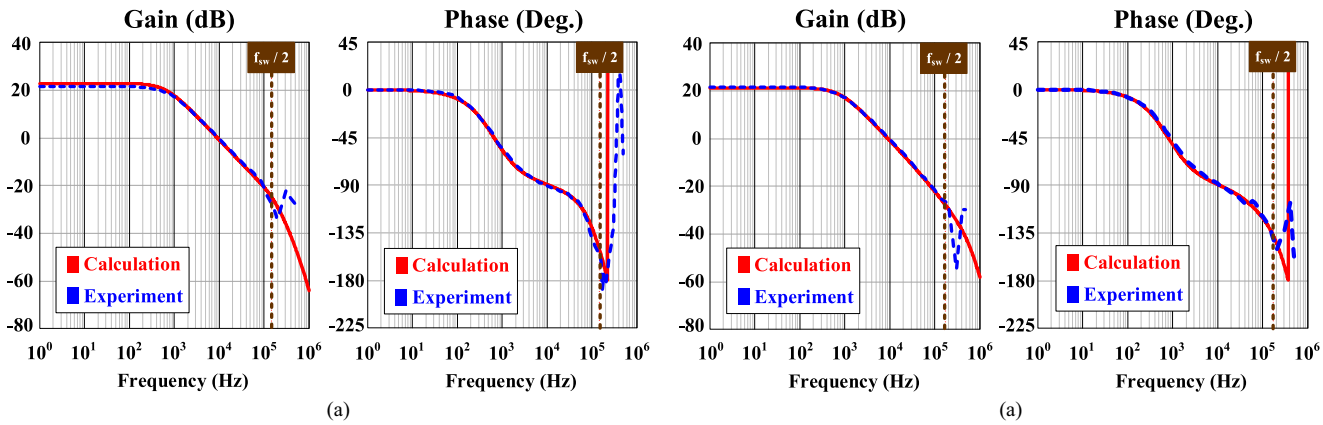

Fig. 17. Control-to-output transfer function results. (a) 12–1.2V (b) 5V–1.2V.

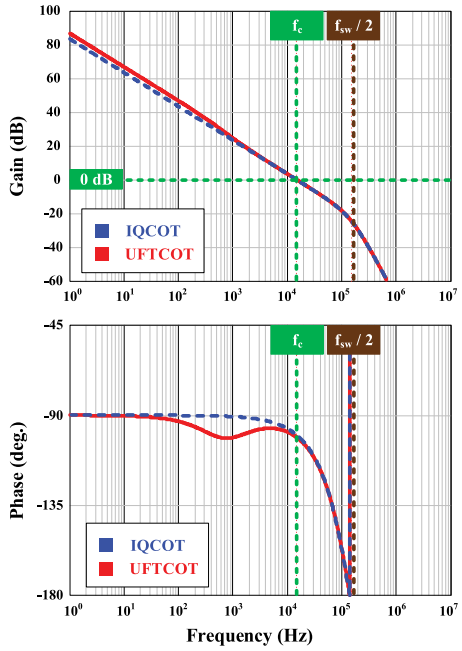

Fig. 18. Loop gain for transient comparison.

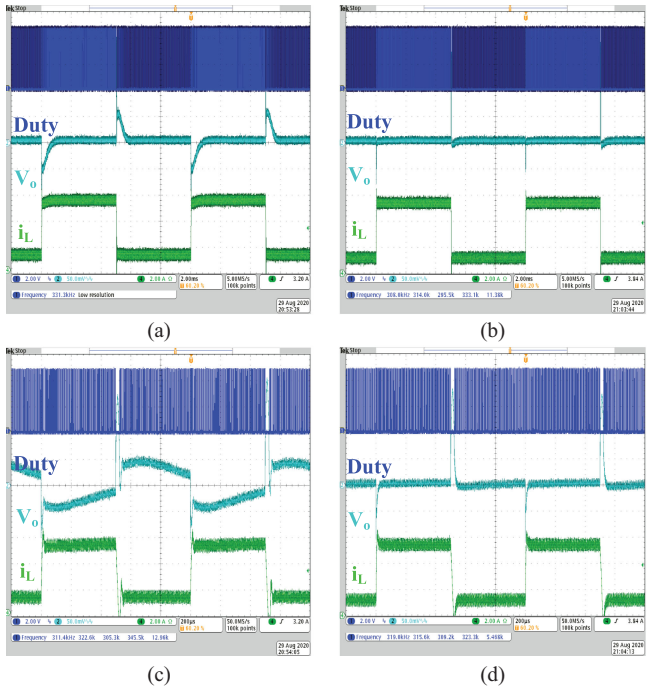

Fig. 19. Dynamic load transient response. (a) IQCOT control @ 100 Hz. (b) Proposed control @ 100 Hz. (c) IQCOT control @ 1 kHz. (d) Proposed control @ 1 kHz.

C. *Load Transient Response Comparison*

The most significant benefit of the proposed control scheme is fast load transient response. To examine its transient performance, the following test conditions are employed: the input voltage is 12 V, the output voltage 1.2 V, and the output current changes from 1 to 6 A. As aforementioned, the load transient is achieved by an on-board transient tool whose slew rate is as high as 50 A/μs to ensure the controller is properly stressed. Note that to have a fair comparison, a PI compensator is applied to make both controls have similar crossover frequency and phase margin. The calculation result is shown in Fig. 18, where the crossover frequency is around 15 kHz and the phase margin is around 75°.

A dynamic load transient with different frequencies is performed, and the results are shown in Fig. 19. When the dynamic frequency is 100 Hz, both the proposed control scheme and IQCOT control can regulate the output voltage at 1.2 V, but the response time of the proposed control is clearly faster than the IQCOT control. Then, as the dynamic frequency is further increased to 1 kHz, the IQCOT control is no longer capable of output voltage regulation, as shown in Fig. 19(c). On the contrary, the proposed control still regulates the output voltage easily, as shown in Fig. 19(d), due to its superior transient performance.

To better quantify the performance, the zoomed-in load transient responses are shown in Fig. 20. Fig. 20(a) shows the transient response of the IQCOT control, whose voltage drop is 102 mV, response time is 6 μs, and settles after 600 μs. On the other hand, for the proposed control, the voltage drop is 53 mV, the response time is 1 μs, and it settles within 20 μs, as shown in Fig. 20(b). Moreover, $V_{th,out}$ in Fig. 20(b) shows a nonconstant

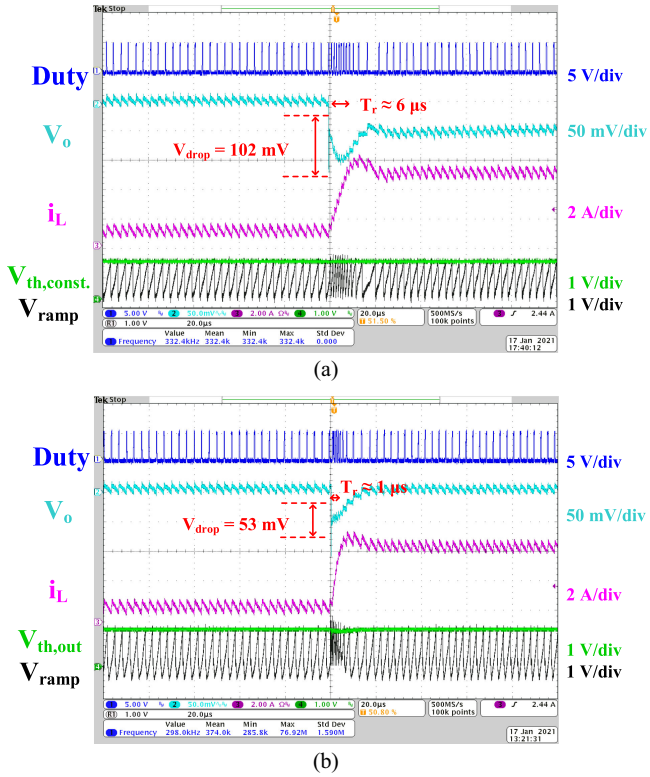

Fig. 20. Load transient response comparison with different control scheme. (a) IQCOT control scheme (b) Proposed control scheme.

threshold voltage during load transients, which is the same as the transient illustration in Fig. 6. Also, it should be noted that because of the internal resistance of the discharge switch, the discharging rate is limited and, hence, V_{ramp} in Fig. 20(b) is not reset to zero in the process of load transient. Clearly, the proposed control scheme is far faster than the IQCOT control scheme.

VI. Conclusion

An ultrafast transient constant on-time (UFTCOT) control is proposed in this article to improve load transient performance while enabling simple multiphase operation. Due to the capacitor current feedback and output voltage threshold, the response time of UFTCOT is 6× faster than IQCOT control. Importantly, thanks to the built-in charging modulation, the instability issue in multiphase operation is readily addressed. Moreover, the small-signal models for UFTCOT control are also derived, providing system design guidelines and verifying its transient performance. Finally, a series of experiments are performed to validate the proposed methods.

References

[1] RichTek, "High efficiency single synchronous buck PWM controller datasheet," *RT8240 A/B/C Datasheet*, 2014.
[2] Y. Hsu, D. Chen, S. Hsiao, H. Cheng, and C. Huang, "Modeling of the control behavior of current-mode constant on-time boost converters," *IEEE Trans. Ind. Appl.*, vol. 52, no. 6, pp. 4919–4927, Nov./Dec. 2016.
[3] J. Li and F. C. Lee, "New modeling approach and equivalent circuit representation for current-mode control," *IEEE Trans. Power Electron.*, vol. 25, no. 5, pp. 1218–1230, May 2010.
[4] J. Li and F. C. Lee, "Modeling of V^2 current-mode control," *IEEE Trans. Circuits Syst. I, Reg. Papers*, vol. 57, no. 9, pp. 2552–2563, Sep. 2010.
[5] S. Tian, F. C. Lee, P. Mattavelli, K. Cheng, and Y. Yan, "Small-signal analysis and optimal design of external ramp for constant on-time V^2 control with multilayer ceramic caps," *IEEE Trans. Power Electron.*, vol. 29, no. 8, pp. 4450–4460, Aug. 2014.
[6] C. Chen, D. Chen, C. Tseng, C. Tseng, Y. Chang, and K. Wang, "A novel ripple-based constant on-time control with virtual inductor current ripple for buck converter with ceramic output capacitors," in *Proc. 26th Annu. IEEE Appl. Power Electron. Conf. Expo.*, 2011, pp. 1488–1493.
[7] T. Qian and W. Wu, "Analysis of the ramp compensation approaches to improve stability for buck converters with constant on-time control," *IET Power Electron.*, vol. 5, no. 2, pp. 196–204, 2012.
[8] S. Bari, Q. Li, and F. C. Lee, "Inverse charge constant on-time (IQCOT) control with ultra-fast transient performance," *IEEE Trans. Emerg. Sel. Topics Power Electron.*, vol. 9, no. 1, pp. 68–78, Feb. 2021.
[9] S. Tian, F. C. Lee, J. Li, Q. Li, and P. Liu, "Equivalent circuit model of constant on-time current mode control with external ramp compensation," in *Proc. IEEE Energy Convers. Congr. Expo.*, 2014, pp. 3747–3754.
[10] S. Tian, F. C. Lee, J. Li, Q. Li, and P. Liu, "A three-terminal switch model of constant on-time current mode with external ramp compensation," *IEEE Trans. Power Electron.*, vol. 31, no. 10, pp. 7311–7319, Oct. 2016.
[11] S. Bari, Q. Li, and F. C. Lee, "High frequency small signal model for inverse charge constant on-time (IQCOT) control," in *Proc. IEEE Energy Convers. Congr. Expo.*, 2018, pp. 6000–6007.
[12] C. Cheng, C. Chen, and S. Wang, "Small-signal model of flyback converter in continuous-conduction mode with peak-current control at variable switching frequency," *IEEE Trans. Power Electron.*, vol. 33, no. 5, pp. 4145–4156, May 2018.
[13] Y. Yan, P. Liu, F. Lee, Q. Li, and S. Tian, "V^2 control with capacitor current ramp compensation using lossless capacitor current sensing," in *Proc. IEEE Energy Convers. Congr. Expo.*, 2013, pp. 117–124.
[14] S. Tian, F. C. Lee, Q. Li, and Y. Yan, "Unified equivalent circuit model of V^2 control," in *Proc. IEEE Appl. Power Electron. Conf. Expo.*, 2014, pp. 1016–1023.
[15] J. Li, "Current-mode control: Modeling and its digital application," Ph.D. dissertation, Virginia Polytechnic Institute and State Univ., Blacksburg, VA, USA, Apr. 2009. [Online]. Available: https://vtechworks.lib.vt.edu/handle/10919/27019
[16] Y. Yan, F. C. Lee, P. Mattavelli, and S. Tian, "Small signal analysis of V^2 control using equivalent circuit model of current mode controls," *IEEE Trans. Power Electron.*, vol. 31, no. 7, pp. 5344–5353, Jul. 2016.
[17] Y. Yan, P. Liu, F. Lee, Q. Li, and S. Tian, "V2 control with capacitor current ramp compensation using lossless capacitor current sensing," in *Proc. IEEE Energy Convers. Congr. Expo.*, 2013, pp. 117–124.
[18] P. Liu, Y. Yan, P. Mattavelli, and F. C. Lee, "Digital V2 control with fast-acting capacitor current estimator," in *Proc. IEEE Energy Convers. Congr. Expo.*, 2012, pp. 1833–1840.
[19] S. Pan, C. Chen, and C. Tsai, "A novel capacitor current constant on-time controlled buck converter at 4-MHz switching frequency," in *Proc. IEEE Energy Convers. Congr. Expo.*, 2018, pp. 6008–6013.
[20] P. Liu, "Advanced control schemes for high-bandwidth multiphase voltage regulators," Ph.D. dissertation, Virginia Polytechnic Institute and State Univ., Blacksburg, VA, USA, Apr. 2015. [Online]. Available: https://vtechworks.lib.vt.edu/handle/10919/52275